We are IntechOpen, the world's leading publisher of Open Access books Built by scientists, for scientists

4,800
Open access books available

122,000
International authors and editors

135M
Downloads

Our authors are among the

154
Countries delivered to

TOP 1%
most cited scientists

12.2%
Contributors from top 500 universities

WEB OF SCIENCE™

Selection of our books indexed in the Book Citation Index in Web of Science™ Core Collection (BKCI)

Interested in publishing with us?
Contact book.department@intechopen.com

Numbers displayed above are based on latest data collected.
For more information visit www.intechopen.com

STM Observation of Interference Patterns near the End Cap and Its Application to the Chiral Vector Determination of Carbon Nanotubes

Tadahiro Komeda[1] and Masayuki Furuhashi[2]
[1]*Tohoku University*
[2]*Osaka Univversity*
Japan

1. Introduction

There is a rising demand for the development of alternative materials used for the electronic devices. This is partially due to the difficulties in a further miniaturization of current silicon-based transistors. Carbon nanotube (CNT) is considered as the most prominent candidate for this purpose (Joachim et al., 2000, Tans et al., 1997, Saito et al., 1998). The electronic property of the CNT can be regarded as a combination of those of a molecule and a solid-state bulk material, which appears as a quantum mechanical behavior at a relatively high temperature including the ballistic conductivity (Javey et al., 2003). The realization of these novel phenomena would be the key for the CNT to be widely used in real applications.

For these demands, it requires precise controls of the electronic states whose size reaches to the spatial structure of the electronic wavefunctions. It cannot be realized without a precise measurement of those properties, but there are not many characterization tools with the required resolution.

Scanning tunneling microscopy (STM) has played an important role in atomic scale characterization. It has been known that the CNT becomes metallic or semiconductive depending on the wrapping of the CNT, which is often cataloged by its chirality. Despite its importance, a technique for its precise measurement is not well established. This is partially because conventional diffraction techniques like as low-energy electron diffraction (LEED) or reflection high-energy electron diffraction (RHEED) cannot be applied to the characterization of molecule like CNT tubes.

The atomic scale resolution of STM enables an estimation of the internal structure of the CNT, which has been employed to the determination of the chirality. However, a precise determination of the chirality is not an easy task. STM can also detect the electronic structure in addition to the structural characterization. A clear example can be seen in the observation of the standing wave formed by the interference of an electronic state of CNT, which is an appearance of the wavefunctions. (Lemay et al., 2001, Venema et al., 1999) Using this technique, the band structure of the CNT has been determined. (Ouyang et al., 2002, Lee et al., 2004)

Here in this chapter, we discuss the STM measurements focusing on the superlattice structures detected near the end-cap of the CNT. We combine high-resolution STM imaging

and several types of simulation methods both for metallic and semiconducting CNT (Furuhashi et al., 2007, Furuhashi et al., 2008).
This study is intended partially for the basic understanding of the mechanism how the interference pattern is formed, unveiling the underlying physics of the complex pattern observed at the end of CNT. Other important issue is an application to the precise determination of the chirality of the CNT. For a determination of the atomic ordering, the analysis of the interference pattern often gives more precise information than the real-space image, as has been demonstrated with other microscopes. We like to apply the observation of the interference pattern near the end of the CNT to the precise determination of the chirality utilizing the sensitivity of the reflection patterns. We like to discuss the possibility of the application of this technique to a precise determination of the chirality of CNT.

2. STM observation of CNT

In this section we show the STM imaging of the CNT, which is usually executed by transferring the CNT on a metal surface. First we describe the experimental procedure for the STM observations. Second we show the actual observed STM images both on the metallic and semiconductive CNT (Furuhashi et al., 2007, Furuhashi et al., 2008).

2.1 Experimental set-up of STM observation of CNT

We performed STM measurement on CNT deposited on an Au(111) surface. The substrate was atomically flat Au(111) thin film which was evaporated on a mica surface at 480°C in a homebuilt evaporation system. The gold surface was cleaned by repeated cycles of Ar^+ sputtering and annealing before CNT deposition in ultra high vacuum (UHV). We confirmed characteristic herringbone reconstruction on the cleaned gold surface by STM. Purified single-wall CNTs (SWCNTs) from Carbon Nanotechnologies Incorporated were used as a sample, which was formed by HiPco method (Nikolaev et al., 1999). After the SWCNTs were dispersed in 1, 2-dichloroethane with ultrasonic agitation for 1h, a droplet of the solution was deposited on the Au(111) substrate in air, which was cleaned in the UHV chamber and take out of it just before the deposition. The sample was then dried with pure nitrogen gas and returned to the UHV chamber. In the UHV condition, the sample was annealed at 220 °C for 1 hour in order to remove residual solvent. (Furuhashi et al., 2007) For the STM measurement, we used JEOL JSTM-4500XT in which the observation was done at liquid nitrogen temperature. STM tips were electrochemically etched W wires, which were annealed at 800 °C in the UHV chamber for the removal of tungsten oxides. Topographic images were obtained by a constant current mode. Current-voltage (*I*-*V*) spectra were taken by recording tunneling current as sweeping bias voltage applied to the sample with feedback-loop opened.

2.2 STM images of CNT

CNT is a graphene sheet wrapped in a cylindrical shape. Thus, in order to discuss the STM image of CNT, we should check the observed STM images of the materials composed of the graphene sheet.
The atomic structure of the graphene layer is illustrated in Fig. 1(a). The unit cell is defined by the two vectors $\boldsymbol{a}_1$ and $\boldsymbol{a}_2$, which includes two carbon atoms. The lengths of both vectors, depicted a hereafter, are $\sqrt{3}$ times of the nearest neighbor distance (nnd) of the carbon atoms (a = 0.246 nm).

The most studied material is the graphite in which the graphene sheets are stacked.

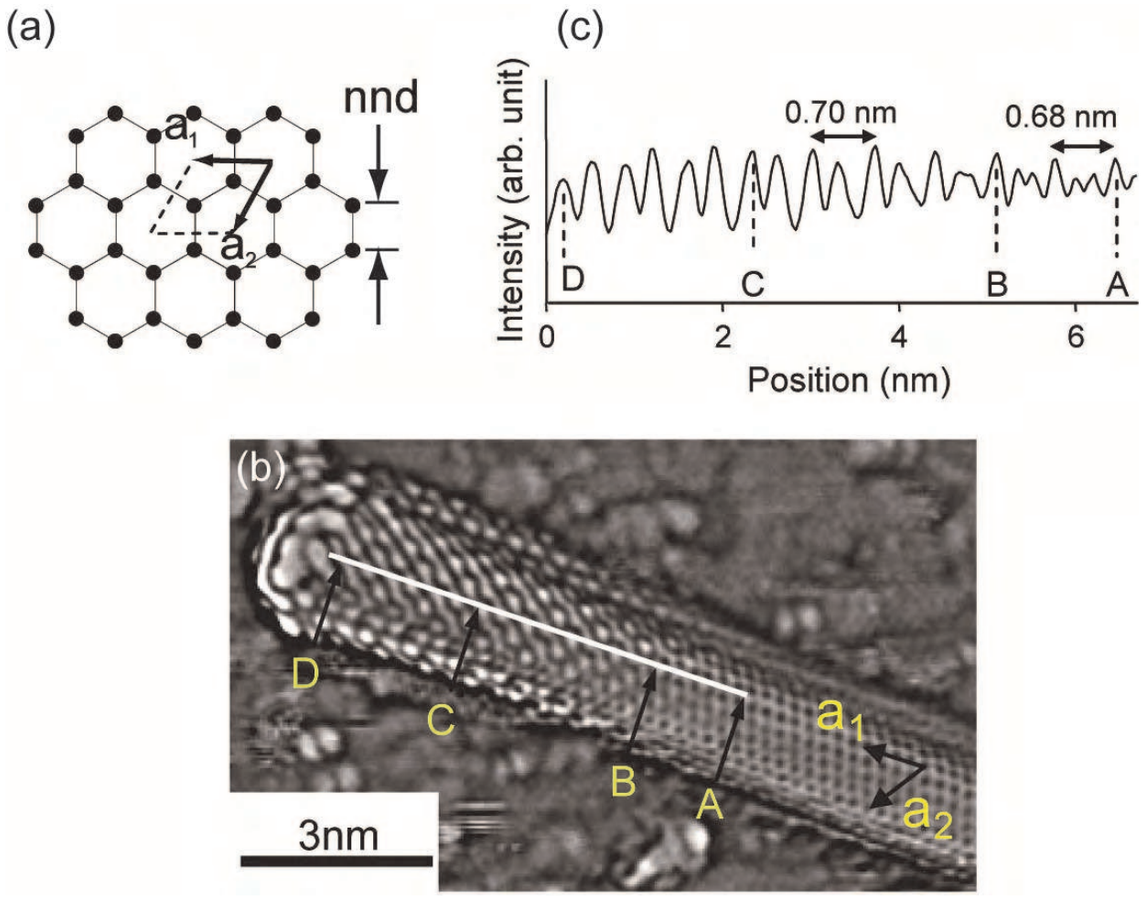

Fig. 1. STM image of armchair-like CNT (a) The atomic structure of the graphene layer. (b) Derivative STM image of a capped (28, -13) nanotube. The letters A, B, C, and D correspond to the positions in (c). (c) The line profile along the highlighted line in (b). A is the starting point of the superlattice structure and two small peaks merge at B. The distance between large peaks in AB is 0.68 nm. The period of paired peaks in BD is 0.70 nm. The intensity of paired two peaks becomes nearly same at C.

Though the carbon atoms are ordered in a honeycomb shape in the graphite layer, the observed STM image shows a close-packed, three-fold symmetry structure. The discrepancy has been explained by the influence of the subsurface layer. The density of states (DOS) at the carbon atom of the top layer changes depending on whether it has a carbon atom just beneath in the second layer. Thus the carbon atoms appear as bright protrusions in an alternative manner in the STM image, forming a three-fold, close-packed structure with a periodicity of a (Batra et al., 1987). In the STM image of the single-layer graphene, such an effect cannot appear and a honeycomb shape structure appears in the STM image.

Figure 1(b) shows an atomically resolved derivative topographic image of a semiconductive CNT, which was taken at 100 pA and 0.6 V. The 'bulk' area shows a periodic grid pattern, where dark spots correspond to the centers of hexagons. The ordering of these spots can be described by using unit vectors (see Fig. 1(a)). Here we define $\boldsymbol{a}_1$ and $\boldsymbol{a}_2$ in the directions

shown in Fig. 1(b). The measured length does not really reproduce expected a, 0.22 nm along $\boldsymbol{a}_1$ and 0.27 nm along $\boldsymbol{a}_2$. The discrepancy from a of 0.25 nm is due to the geometrical configuration of STM tip and cylindrical CNT surface in which the carbon atoms are positioned on a curved surface (Venema et al., 2000, Meunier et al., 1998). Since a slight geometrical difference is not important in our discussion, no correction of the distortion of the STM images was executed. The end of the CNT has a round shape, and is probably capped by one of the hemispheric fullerene family members.

Characteristic parallel wavy lines appear within 6−7 nm from CNT end. The height-profile is measured along the line A-D which is parallel to $\boldsymbol{a}_1$ (see Fig. 1(c)). In the region between A and B, we see a characteristic features, i.e., two small peaks were sandwiched between larger peaks. These small peaks become merged in the region between B and D. The periodicity of the large peaks is ~0.68-0.70 nm in the whole region, which should correspond to ~3a. We consider the periodicity is derived from the Fermi wavelength, which is estimated as three times of the unit vector of the graphene (Saito et al., 1998).

Figure 2(a) shows an enlarged image of Fig. 1(b) at the interface region of the superlattice and the bulk. The positions of carbon atoms in the superlattice can be clearly identified from the carbon hexagons in the bulk region. We see superlattice structures in the CNT image, which is schematically illustrated in Fig. 2(b). The structures can be described by a combination of cranked lines and oval-shape spots, which were sketched by grey lines and white ellipses, respectively, in Fig. 2(b). The trace of the line has the same shape as that can be seen in the edge of the ideal armchair CNT. The direction of the cranked line is parallel to the 'armchair direction' which is marked in Fig. 2(b). The periodicity of the ovals along this direction is $\sqrt{3}a$. A similar superlattice structure with the same periodicity was reported in the STM images obtained near a particle and an edge on graphite surface (Xhie et al., 1991, Kobayashi et al., 2005).

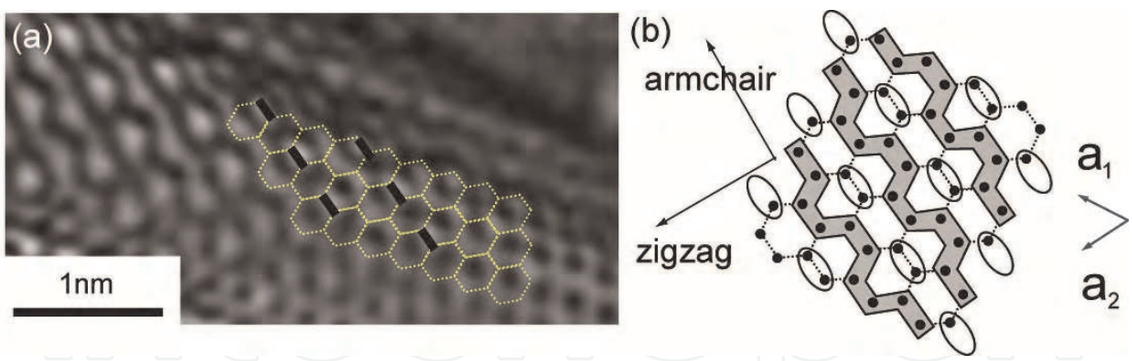

Fig. 2. Magnified image of Fig. 1(b) (a) Enlarged image of the point B in Fig. 1(b). The dotted lines mean the honeycomb structure of primitive graphene. The ellipses are emphasized by thick bars. (b) Diagram of the relation between the positions of carbon atoms and the apparent structure in (a). The black circles represent carbon atoms, and the arrows indicate the $\mathbf{a}_1$ and $\mathbf{a}_2$.

We measured another semiconductive CNT, whose image was obtained with the conditions of 0.6 V and 100 pA (see Fig. 3(a)). In this image, two CNTs are overlapped with each other, and we show the border of two CNTs by the dashed line in Fig. 3(a). Due to the conditions of the STM tip, the two CNTs were convoluted into a single tube in the image. However, low bias dI/dV mapping image can clearly distinguish the two CNTs (inset figure). The

mapping image was obtained by plotting a derivative conductance at −0.4 eV which was detected by using a lock-in amplifier, while the tip scanned the surface with a closed feedback-loop (modulation voltage was superimposed on the sample voltage, which was small enough to obtain a decent topographic image). We assign the upper CNT as (11, 4) or (12, 4), whose chiral angle is between armchair and zigzag nanotubes. The ambiguity of the chiral vector is due to the error bar of the measurement of the diameter.

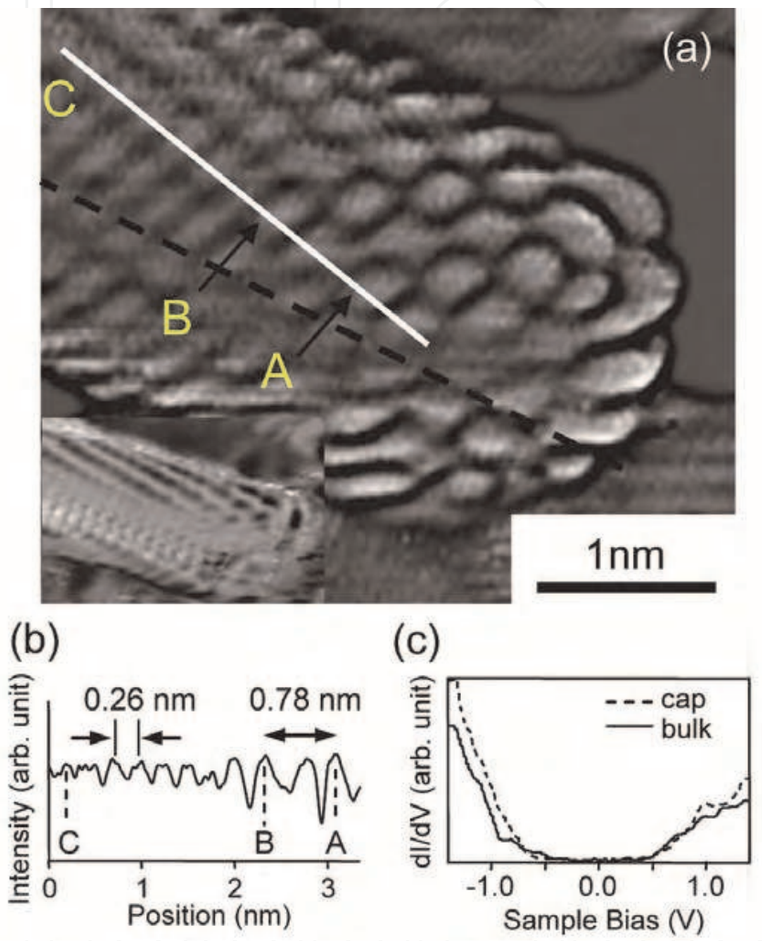

Fig. 3. STM image of semiconductive CNT (a) Derivative STM image of two nanotubes ends. The dashed line represents the border of nanotubes. Ellipse rows and cranked lines are observed. (inset) the dI/dV mapping image of the same nanotubes at -0.4 eV. (b) The line profile along the highlighted line in (a). AB corresponds to the distance between ellipse rows in (a), and the point C is on the normal period. (c) dI/dV-V spectra on the cap (dashed line), and on the bulk (solid line) where is 5 nm far from the end.

The combination of the oval-shape spots and the cranked lines can be observed near the end-cap, which is similar to the ones observed for the CNT of Fig. 2(a).
Figure 3(b) shows the height-profile along the line A-C in Fig. 3(a). The distance between A and B is ~ 0.78 nm, which is close to 3*a*. The superlattice structure appears in a limited area from the end-cap. The dI/dV curves measured on the cap and the bulk are shown in Fig. 3(c). The band gap was observed on both sites, indicating that they are both semiconductive.

The van Hove singularities were weak and can not be assigned. The electronic states detected with the condition of the sample bias of 0.6 eV correspond to the ones at the edge of the conduction band. The band gap of this CNT expected from a theoretical calculation is ~0.7 eV, which was deduced from the equation of $E_{gap}=2|\gamma_0|a_{c\text{-}c}/d$ (Saito et al., 1998), where γ_0 = -2.7 eV corresponding to the C-C overlap energy, $a_{c\text{-}c}$ = 0.142 nm is the nearest neighbor distance between carbon atoms, and d = 1.1 nm is the diameter of the CNT.

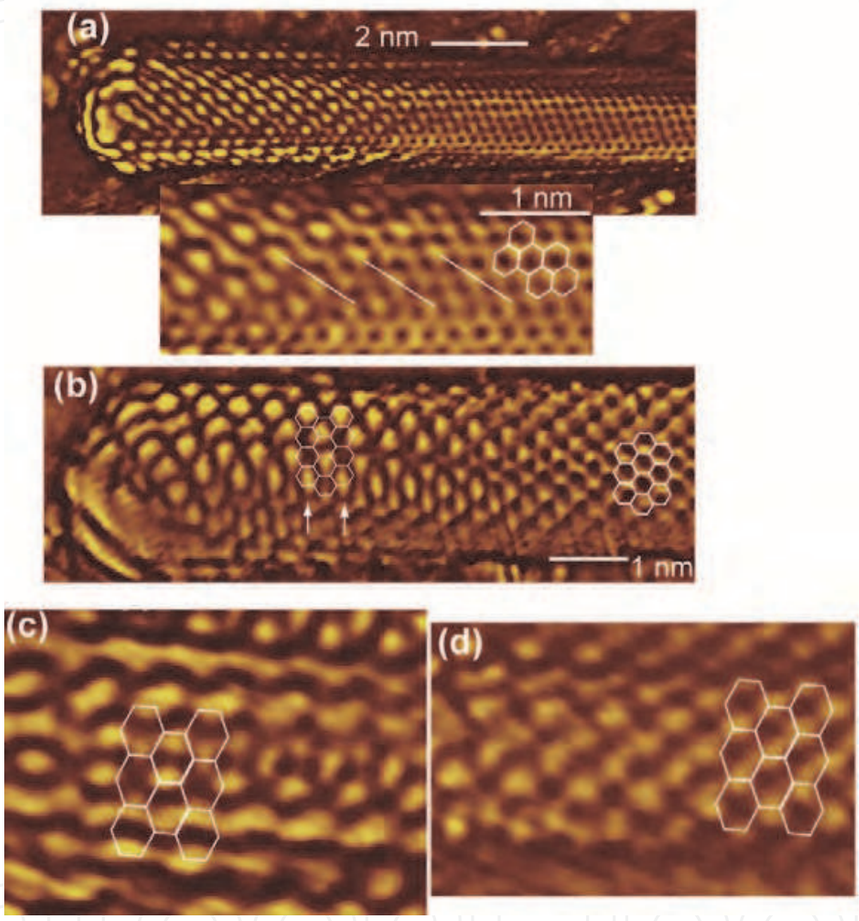

Fig. 4. Comparison of STM images of armchair and zigzag CNT (a) Upper panel: Interference pattern observed near the end-cap of armchair-like semiconducting CNT (chiral vector (28, -13)), (I_t = 100 pA V_{bias} = 0.6 V). Lower panel: Magnified image of the upper panel. The thin lines are included as a guide to the eye for the aligned bright spots. The superlattice structure imposed hexagons are the primitive honeycomb structures. (b) Interference patterns for the zigzag CNT (I_t = 100 pA V_{bias} = 0.7 V). Bright spots separated by 4***a*** along the arrows. (c)(d) Bias dependence of an interference pattern of the zigzag CNT measured with I_t = 100 pA and (c) V_{bias} = 0.7 V , (d) V_{bias} = 1.0 V at an identical position of the same CNT(chiral vector (15,-1)).

The band gap estimated by the onsets of the dI/dV curve is in the range of 0.9-1.0 eV, which is larger than the theoretical prediction. Similar discrepancies are reported previously which should be due to the band broadening.

Near the end-cap of the CNT, we can find a report that detected a gap-state (Kim et al., 2005). However we could not see a similar state. Instead we detect a small energy shift (~ 0.1 eV) to the higher sample bias in the dI/dV spectrum at the end-cap region compared to that observed at the normal region.

Here we compare the structure at the end-cap of the armchair and the zigzag CNT in Fig. 4. The images are shown in a derivative manner to flatten the background. In the upper panel of Fig. 4(a), the end-cap is positioned on the left hand side and the infinite tube extends to the right. We can estimate a chiral angle of ~2.9° and a tube diameter of ~1.9 nm, from which the most plausible chiral vector of (28, -13) can be deduced. Since this CNT is close to an armchair type, the CNT axis is close to the ΓK direction in $\boldsymbol{k}$ space.

Near the end-cap, we observe a characteristic structure with a complex pattern. This structure can be described as a combination of aligned bright spots and wavy lines sandwiched by the former. The alignment is indicated by thin lines in the figure, which are rotated 60° from the tube axis. The wavy patterns are also aligned along the thin lines. The separation of the bright spots (pointed by upper-ends of the bars) along the CNT axis is ~ 0.68-0.70 nm that is close to $3a$. This agrees with the interference periodicity discussed in metallic CNTs (Lemay et al., 2001, Ouyang et al., 2002, Rubio et al., 1999), wherein the energy band crosses the Fermi level at the K point that corresponds to $\boldsymbol{k} = 2\pi/3a$, which is the origin of the periodicity of $3a$.

When the chirality of the CNT is close to zigzag, the STM image near the end-cap is like the one shown in Fig. 4(b). Similar to the case of Fig. 4(a), a complex pattern can be observed within ~6 nm from the end-cap. In the right-hand side area, we can see a hexagonal network rotated 30° from the armchair direction. The CNT axis is aligned to the ΓM direction of the Brillouin zone. On the left-hand side, we can notice a pattern of bright spots with a large periodicity perpendicular to the tube-axis. Along the thin-arrows, we note bright spots with a separation of ~$4a$ (see superimposed hexagons). Along a line between the two, two bright spots are separated by a.

We show STM images of another zigzag CNT in Fig. 4(c) that was imaged with a condition of V_{bias} = 0.7 V, which exhibits more minute features. We assigned the chirality of the CNT as (15, -1) which is close to the zigzag but different from the one of Fig. 4(b).

When the same CNT was observed with V_{bias} = 1.0 V, the image shows a 1×1 pattern even near the end-cap. This is shown in Fig. 4(d), which was obtained in the same area with that of Fig. 4(c). This is caused primarily by a mixture of various electronic states contained in the allowed energy region.

3. Simulation of STM images of CNT

The electronic property of the CNT is partially determined by how it is wrapped from the graphene sheet, whose unit vectors of $\boldsymbol{a_1}$ and $\boldsymbol{a_2}$ are shown in Fig. 5(a). The wrapping is characterized with a chiral vector $\boldsymbol{C}$ and translational vector $\boldsymbol{T}$. The tube axis is parallel to the latter which is perpendicular to the former.

The chiral vector is expressed with a form of $\boldsymbol{C_h}=n\boldsymbol{a_1}+m\boldsymbol{a_2}$, which is often denoted as (n, m) (see Fig. 5(a)). Two symmetry lines are often referred in the chiral vector discussion, and are called armchair and zigzag direction which are shown in Fig.5 (a). The chiral angle (ϕ) is defined as the angle between the chiral vector and the armchair direction. The CNT with $\phi=0°$ is called an armchair CNT and the one with $\phi=30°$ is called a zigzag CNT.

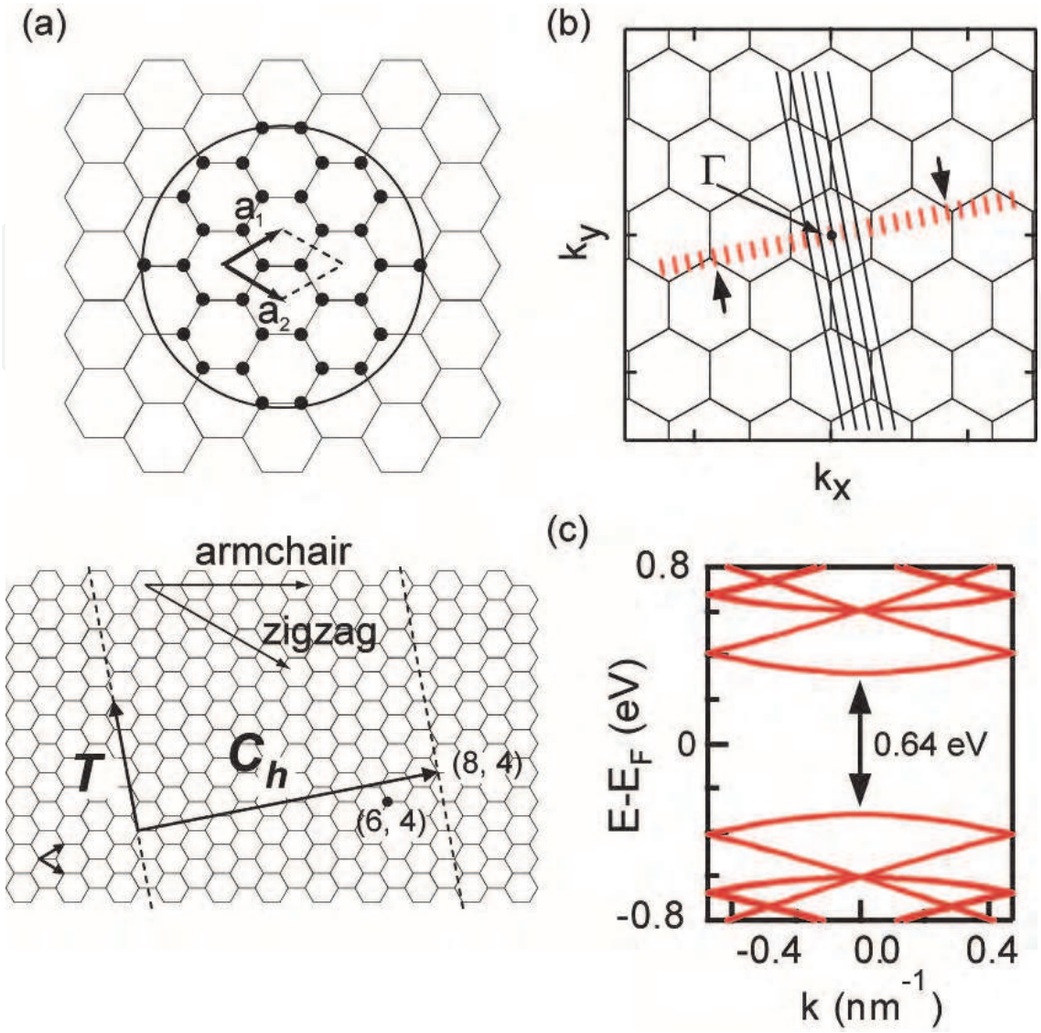

Fig. 5. Chiral vector and band structure of CNT (a) (upper) atomic structure of a graphene layer. The carbon atoms are indicated by solid circles, and a unit cell is indicated by two unit vectors and dashed lines which contains two carbon atoms. 34 atoms in the circle are used for the calculation of electron probability for the STM simulation. (lower) Definition of chiral vector $\boldsymbol{C}_h$ and translational vector $\boldsymbol{T}$ of carbon nanotube. (b) Brillouin zones of graphene and allowed $\boldsymbol{k}$ points for the (4, 2) CNT that are marked by the long black lines. The short red lines are equivalent to them. The k points that give the energy minimum (maximum) in the conduction band (valence band) are indicated by arrows, which are the closest points to K and K'. (c) Calculated band structure for a CNT of (15,-1). The length along the horizontal axis corresponds to the length of the red lines in (b).

Though the electronic structure of a CNT is close to that of graphene, limited $\boldsymbol{k}$ points are allowed due to quantization of an electron in the wrapping direction. The allowed $\boldsymbol{k}$ points can be plotted on straight lines along the tube axis direction, separated by $2\pi/|\boldsymbol{C}_h|$ from each other. In Fig. 5(b), we show an example of such lines for a CNT with a chirality of (4, 2). These are shown by long black lines. An equivalent expression is a series of short bars whose lengths are an inverse of the translational vector, which are also shown in Fig. 5(b) by

the short red lines. It has been demonstrated that if the chiral vector (n, m) satisfies the condition of n-m=0 (mod 3), the CNT is metallic and the energy band (E(k)) curve crosses the Fermi level at K or K'. For a semiconducting CNT, the lines of the allowed $\boldsymbol{k}$ vectors never cross the K point. The minimum (maximum) energy in the conduction (valence) band is given at $\boldsymbol{k}_{min}$, which is on the red lines and is closest to the K or K' point (White et al., 1998). In Fig. 5(b), we show the positions of $\boldsymbol{k}_{min}$ with arrows.

The band structure can be calculated using the standard formula, and the result for (15, -1) is shown in Fig. 5(c). The length of the x-axis corresponds to that of the short red lines in Fig. 5(b), and the valence band maximum and conduction band minimum is given at $\boldsymbol{k}_{min}$, which has an energy gap as expected from a semiconducting nature of the CNT.

Kane *et al*. discussed that the symmetry breaking might occur at semiconductive tube end in STM image. This is because that the incoming and back-scattered electron waves might be interfered near the end, and break the rotational symmetry. The expected interference pattern was 1×1 spiral stripes, which ran along the zigzag direction of nanotube (Kane et al., 1999). However, the patterns near the end-caps shown above are not simple stripes. Moreover, they are along the armchair direction instead of the predicted zigzag direction. These superlattice structures could not be explained by a simple electron wave scattering theory. Rubio *et al*. calculated molecular orbitals and STS images of an armchair nanotube with a finite length by density-functional theory method (Rubio et al., 1999). One of the orbitals in the Hückel catalog near the Fermi level has a similar pattern to that of Fig 2(b), which was obtained near the interface area. The STM image of the metallic CNT near the Fermi level was calculated by the combination of the four patterns at K point on the Brillouin zone of nanotube. Indeed, the dI/dV mapping image of the nanotube with 30 nm length equaled to the shape of wavefunction because the small length made the energy levels discrete by quantum size effect (Lemay et al., 2001). The observed wavefunctions were the combination of Bloch functions and equaled to the molecular orbitals.

We examine two types of the calculation focusing on the simulation of the symmetry breaking patterns observed neat the cap end.

3.1 Simulation by molecular orbital calculation

First we show a simulation with using molecule orbital calculation. We calculated the molecular orbitals of capped nanotube by PM3 method (Stewart, 1989, Stewart, 1989, Stewart, 1991). The calculation was carried out by MOPAC2000 package (Stewart, 1990). We employed a model nanotube (10, -4) instead of (28, -13) latter of which was actually shown in the STM observations. This is because of the limitation of our computational resource. Because the nanotube (10, -4) has an apparent chiral angle (ϕ) of 6.6 ° which is close to ϕ=2.9° observed for the (28, -13) CNT. Thus we believe the calculation can reproduce the experimental results. The calculated HOMO and LUMO orbitals are shown in Fig. 6(a) and (b), respectively. The distribution of LUMO orbital shows clear ellipses and cranked-lines along the armchair direction, which is similar to the image of Fig. 2(b). The distance between the ellipses along the zigzag direction is 3a. On the other hand, the distribution of HOMO does not show the cranked-line, whereas circles are visible along the armchair direction. The STM image obtained with a positive sample bias corresponds to the distribution of an unoccupied electronic state; therefore the theoretical simulation above reproduces the observed STM images.

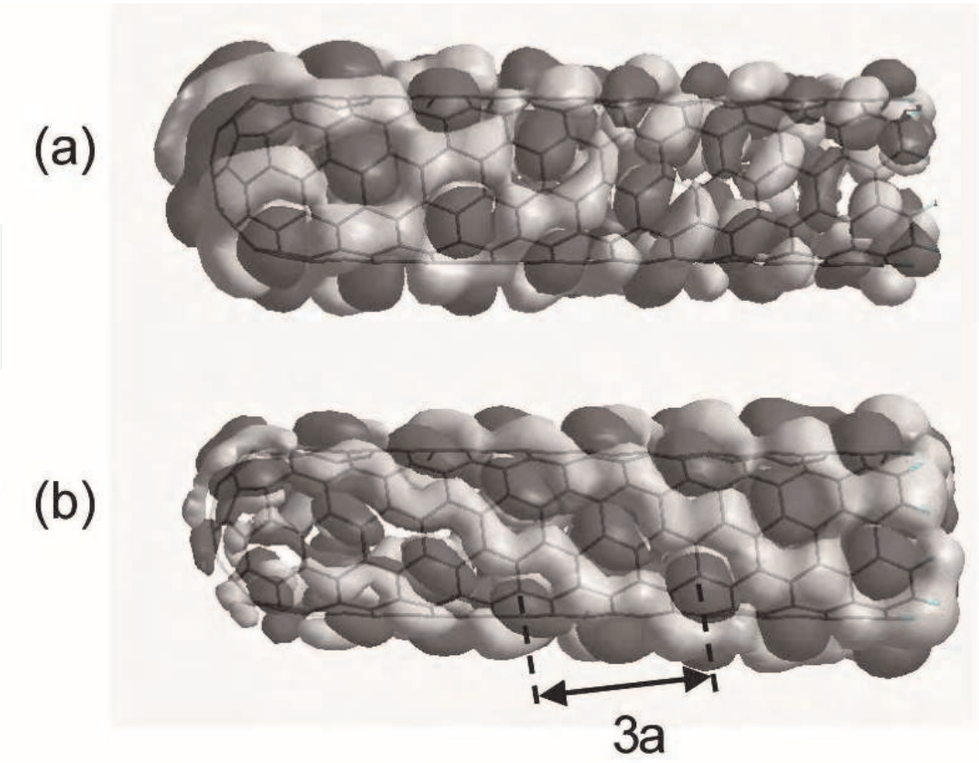

Fig. 6. STM image of CNT simulated by PM3, molecular orbital method (a) HOMO and (b) LUMO calculated by PM3 method. The nanotube consists of 220 carbon and ten hydrogen atoms. The grey-scale tone corresponds to the sign of phase. The left side is capped by a hemisphere of carbon atoms, and the right side is terminated by hydrogen atoms. The wave length along the apparent chiral angle direction is indicated by an arrow.

In addition, further information can be obtained from Fig. 6. The local density of states, ρ_{LDOS}, can be expressed by the following equation:

$$\rho_{\mathrm{LDOS}}(\mathbf{r}, E) = \sum_i \left|\psi_i(\mathbf{r})^2\right| \delta(E_i - E) \,, \tag{1}$$

where ψ_i are the wavefunction with the eigenvalue E_i, and i corresponds to the index of eigenstates. It is obvious that the electron population can be estimated with the LDOS of the atom at the position. It is measured that the HOMO has a larger population at the cap than at the normal part, whereas the LUMO behaves in an opposite manner. This is why the pentagon in the cap works as electron acceptor. It is due to the Hückel rule that the cyclic π-electron state containing $4n + 2$ electrons is the most stable one (n is an integer). The carbon pentagon contains five π-electrons in the neutral state, and tends to attract a single electron. Therefore a negative charge is localized near the cap.

The change of the charge distribution causes a band bending, and the occupied states at the end-cap should be shifted downward. We consider that this can account for the energy shift of the dI/dV spectrum shown in Fig. 3(c). We conclude that the modulated pattern was observed when the STM sample bias agreed with the bottom of the conduction band whose energy level was shifted due to the band bending.

3.2 Simulation by Bloch theorem

Now we discuss a simulation based on Bloch theorem. We first examine the electronic structure of the graphene sheet (Saito et al., 1998). The unit cell of the graphene includes two carbon atoms (A and B in Fig. 5(a)). In the tight-binding approximation, Bloch function is given by a linear combination of atomic orbitals (LCAO). In a case of the π-electron system, we only have to consider p_z orbital, and the one-electron wavefunction is obtained by a linear combination of the p_z Bloch functions:

$$\psi(\mathbf{k},\mathbf{r}) = \frac{C_A}{\sqrt{N}} \sum_{\mathbf{R_A}}^{N} e^{i\mathbf{k}\cdot\mathbf{R_A}} \varphi_A(\mathbf{r}-\mathbf{R_A}) + \frac{C_B}{\sqrt{N}} \sum_{\mathbf{R_B}}^{N} e^{i\mathbf{k}\cdot\mathbf{R_B}} \varphi_B(\mathbf{r}-\mathbf{R_B}), \tag{2}$$

where $\boldsymbol{R_A}$ and $\boldsymbol{R_B}$ indicate coordinates of the carbon atom A and B, respectively. C_A and C_B are normalization coefficients, and φ depicts atomic orbitals. The details of the calculation about overlap integrals and eigenvalue were discussed by Saito and Dresselhaus (Saito et al., 1998). When we assume the overlap integral to be zero, the eigenvalue becomes $E(\boldsymbol{k}) = \pm t\omega$, where t is the overlap energy integral and ω is defined below. The normalization coefficient becomes $C_B = \pm(f^*/\omega)C_A$. Here f^*/ω can be depicted as $Ae^{i\theta}$ ($A \geq 0$), and $|f^*/\omega|^2 = A^2 = 1$. The wavefunction can be deduced as following:

$$\psi_{\pm}(\mathbf{k},\mathbf{r}) = \frac{C(\mathbf{k})}{\sqrt{N}} \left[\sum_{\mathbf{R_A}}^{N} e^{i\mathbf{k}\cdot\mathbf{R_A}} \varphi_A(\mathbf{r}-\mathbf{R_A}) \pm \sum_{\mathbf{R_B}}^{N} e^{i(\mathbf{k}\cdot\mathbf{R_B}+\theta)} \varphi_B(\mathbf{r}-\mathbf{R_B}) \right], \tag{3}$$

where

$$\begin{aligned} \cos\theta = \mathrm{Re}\frac{f^*}{\omega} &= \frac{1}{\omega}\left(\cos\frac{k_x a}{\sqrt{3}} + 2\cos\frac{k_x a}{2\sqrt{3}} \cos\frac{k_y a}{2} \right), \\ \sin\theta = \mathrm{Im}\frac{f^*}{\omega} &= \frac{1}{\omega}\left(-\sin\frac{k_x a}{\sqrt{3}} + 2\sin\frac{k_x a}{2\sqrt{3}} \cos\frac{k_y a}{2} \right), \end{aligned} \tag{4}$$

and

$$f = e^{ik_x a/\sqrt{3}} + e^{-ik_x a/2\sqrt{3}} \cos\frac{k_y a}{2}, \tag{5}$$

$$\omega = \sqrt{f f^*} = \sqrt{1 + 4\cos\frac{\sqrt{3}k_x a}{2}\cos\frac{k_y a}{2} + 4\cos^2\frac{k_y a}{2}}, \tag{6}$$

Eq. (3) gives a wavefunction with the wavevector $\boldsymbol{k}$ as a parameter, whose value is determined by the periodic boundary condition of each carbon nanotube. We treat C as a constant value that is independent of $\boldsymbol{k}$ for simplicity.

The tunneling current I_t is proportional to the integrated LDOS between the Fermi level and the applied bias voltage V (here the LDOS of the tip is neglected):

$$I_t(\mathbf{r}, eV) \propto \int_{E_F}^{E_F+eV} \rho_{LDOS}(\mathbf{r}, E) dE. \tag{7}$$

The thermal broadening of the Fermi level is ignored. Since the electronic states that contribute to the tunneling current are located in the energy region close to the Fermi level and the band edge, we can simplify the integration in eq. (7). For a simulation of the STM images, we estimate a space distribution of the tunneling current in the logarithmic scale assuming the tip scans at a certain constant height. This is due to a limited calculation resource.

In order to estimate the probability that one can find the electron at $\boldsymbol{r}$, we have to consider the contributions from $2N$ atomic orbitals. However, the contribution decreases exponentially with the tip-surface distance. Hence, we consider only the 34 atoms close to the tip position [illustrated in Fig. 5(a)].

First, we show the simulation without the interference for a metallic, (5, 5) armchair CNT. As shown in Fig. 7(a), there are two symmetric sets of crossed energy dispersion curves (E vs $\boldsymbol{k}$) at the Fermi level in the infinite CNT. In the 'normal' region (where the electronic structure is not affected from the end or defect), the topographic image is formed by integrating the tunneling current from the four dispersion curves of Fig. 7(a).

Figure 7(b) shows a topographic image of the CNT at 20 meV above the Fermi level, where the CNT axis is set to the horizontal line. We have confirmed that the image obtained at 20 meV below the Fermi level has a similar distribution. The pattern shows a simple 1×1 hexagonal structure, which seems to reproduce the positions of the carbon atoms. However, this pattern is the superposition of two superlattice structures that have different symmetries. We illustrate two patterns in Fig. 7(c) and (d), which correspond to the square of the wavefunctions on curve I and II, respectively (the wavefunction in III and IV give completely same electron probability with II and I, respectively).

In the images, the real part of the wavefunctions is superimposed as circles whose size and colors correspond to the amplitude and the phase, respectively.

We see a periodic variation in the amplitude of the real part of the wavefunctions along the nanotube axis (horizontal direction in the figures), whose periodicity is ~ $3a$ both in Fig. 7(c) and (d). However, as can be seen in the blue and red distribution, the phase is reversed for half of the carbon atoms in the image. The superposition of the tunneling current makes an isotropic hexagon pattern illustrated in Fig. 7(b).

Similar simulations of the STM image of the metallic CNT have been performed previously. Meunier and Lambin calculated STM image of metallic nanotube and shows a good agreement with our image except for a small anisotropy that is purely originated from geometric distortion around circumferential direction (Meunier et al., 1998, Meunier et al., 2004). As far as we consider defect-free CNT, it is expected that the 1×1 sixfold hexagon structure always appears in the topographic image of metallic CNT. We like to note that this is because STM can only measure the superposition of the multiple contributions, and cannot distinguish the four dispersion curves.

Next, we show the topographic image generated by the interference of the wavefunctions.

One-dimensional interference wavefunction can be expressed by a superposition of the forward and backward waves that has an equivalent electron energy (Ouyang et al., 2002). A two-dimensional interference pattern can be generated by using eq. (3):

$$\rho_{LDOS} \propto \left| \psi(\mathbf{k}_1, \mathbf{r}) + R\, \mathrm{e}^{i\eta} \psi(\mathbf{k}_2, \mathbf{r}) \right|^2 , \tag{8}$$

where η and R are a phase shift and a reflectivity, respectively. These parameters are determined how the waves are reflected at the terminal and the defect.

In Fig. 8(a), we show the simulation result assuming R= 1 and η= 0°. The rows of emphasized dimers can be seen along the vertical direction. Between these rows, there are cranked-lines with a weak intensity along the vertical armchair direction. The distance between dimers along CNT axis is $3a$, which makes a $\sqrt{3}\times\sqrt{3}$ superlattice structure. Figure 8(a) shows a good agreement with previous calculation and measured STM image (Kane et al., 1999, Clauss et al., 1999).

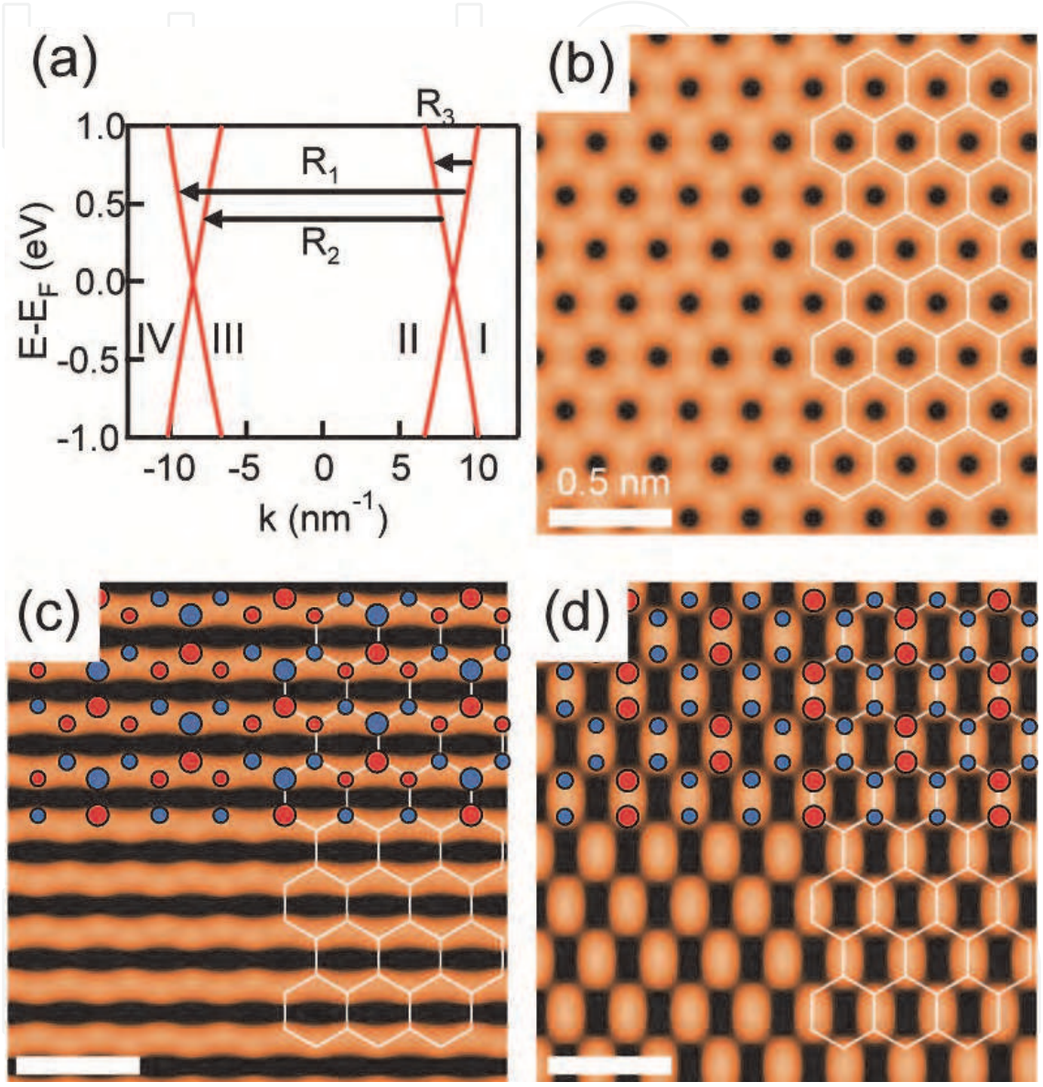

Fig. 7. Simulated STM image of CNT by Bloch theorem. Simulation of (5, 5) armchair carbon nanotube. (a) Energy dispersions near the Fermi level. The k is the 1D wavevector, which is the part of 2D wavevector $\boldsymbol{k}$ along nanotube axis. The R1, R2, and R3 indicate possible reflection paths. (b) Simulated STM image without interference at 20 meV above Fermi level. The highlighted lines represent primitive honeycomb structure. (c) and (d) are electron distributions with schematic images of wavefunctions on curve I and II at 20 meV above Fermi energy, respectively. The uppers are the superposed real parts of wavefunctions, whose circle size and color represent the value of LCAO coefficient and the sign of phase, respectively.

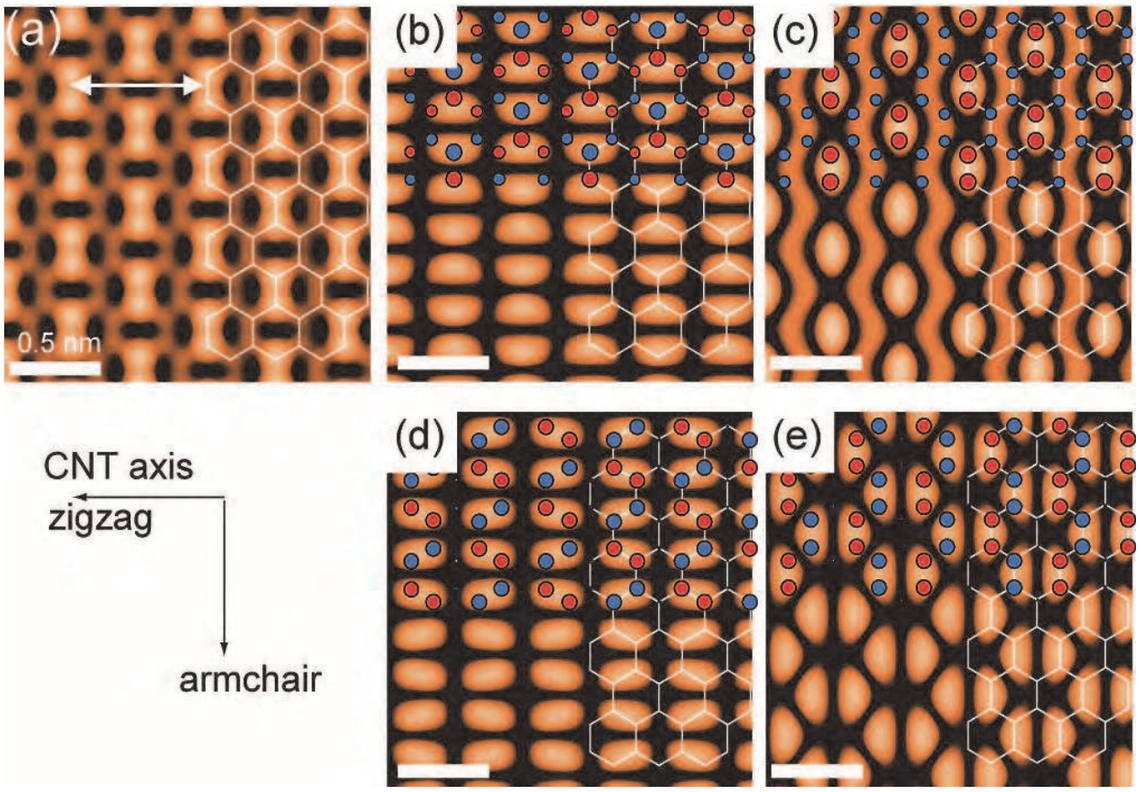

Fig. 8. Interference topographic image of armchair CNT (a) Interference topographic image of a (5, 5) armchair carbon nanotube at $E(k)$ = 20 meV, R = 1 and η = 0. The white arrow indicates 3a. The images of (b) and (c) correspond to the reflection R_1 and R_2 at η = 0, respectively. The real parts of wavefunction are superposed on upper region. (d) and (e) are the same images with (b) and (c) substituting $\eta = \pi$, respectively. The imaginary parts of wavefunctions are illustrated on upper region.

In order to analyze the contribution from the reflection path indicated in Fig. 7(a), we divide the image of Fig. 8(a) into two interfered waves corresponding to the reflection path of R_1 and R_2, which are shown in Fig. 8(b) and (c), respectively. (η = 0) The obtained patterns also have $\sqrt{3}\times\sqrt{3}$ superlattice structures. We also check interference pattern variation with the phase shift η. We show examples for the case of $\eta = \pi$ in Fig. 8(d) and (e). However, the superposition of Fig. 8(d) and (e) does not reproduce the experimental STM images, whose reason is not clear at this moment.

These interference images give a similarity with molecular orbitals (MOs) in a finite length metallic nanotube near the Fermi level as we have shown above (Lemay et al., 2001, Rubio et al., 1999). It suggests that all simulated scattering can occur by the condition of the reflection. In addition, several groups discussed about electron wave scattering in an armchair nanotube (Kane et al., 1999, Yaguchi et al., 2001), and considered two scattering ways, which are inter-valley (R_1 and R_2) and intra-valley (R_3) reflection. Inter-valley reflection occurs with the phase shift of 0 and π. We consider that the actual interference image becomes complex superposition of the standing wave patterns with various phase shifts.

Moreover, we have simulated the topographic image of a semiconductive CNT. As shown in Fig. 9(a), a semiconductive CNT has a band gap and the energy dispersion curve is

symmetric around the top and bottom of the band gap. Figure 9(b) gives a magnified image of the conduction band edge in Fig. 9(a). Figure 9(c) and 9(d) show images at the edges of the conduction band and the valence band of the (6, 4) CNT, respectively. The CNT axis is aligned to the horizontal line. Both images shows a 1×1 striped spiral pattern that runs along a zigzag direction and $\pi/3$ rotation with respect to each other. These features are consistent with the report of Kane and Mele (Kane et al., 1999).

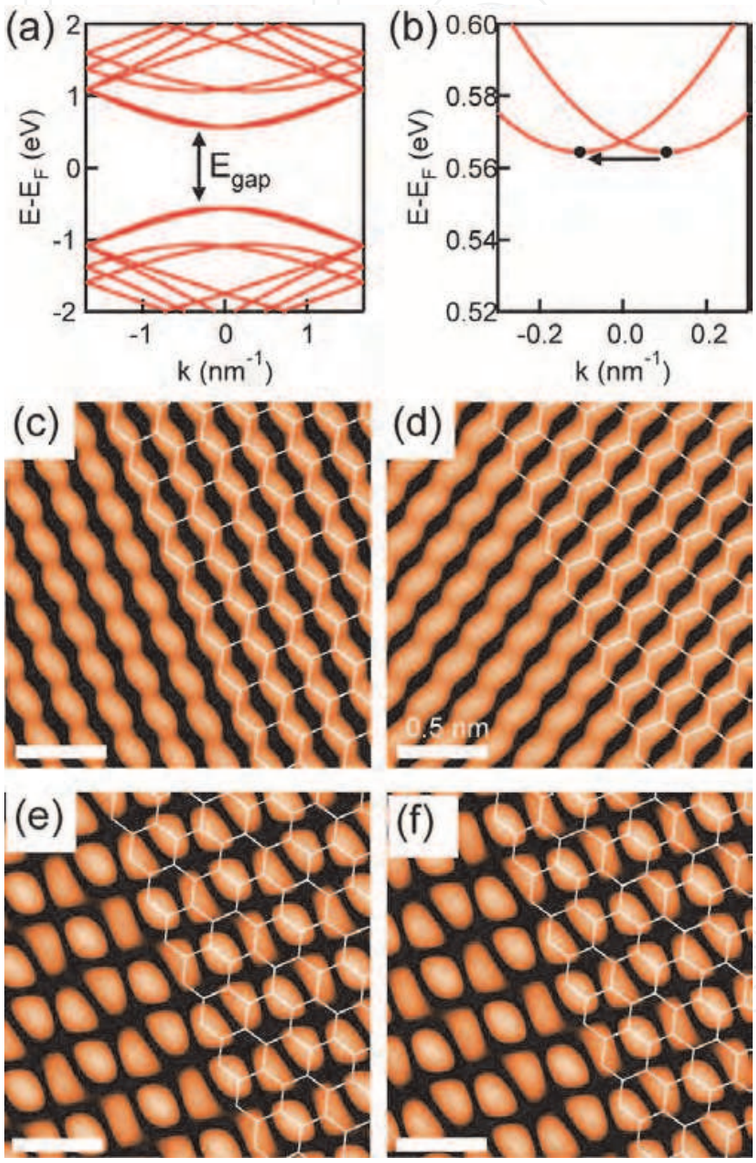

Fig. 9. Dispersion curve of semiconductive CNT and interference pattern (a) Energy dispersion curve of (6, 4) semiconductive nanotube. The band gap is defined as the difference between conduction band bottom and valence band top. (b) Magnified image of (a) near the conduction band bottom. The black dots indicate the energy bottom position. (c) and (d) are simulated topographic images at conduction band edge and valence band edge, respectively. The interference images at (e) $\eta = 0$ and (f) $\eta = \pi$ shows similar patterns.

At the band edge, there are only two wavefunctions that contribute to the tunneling current which have an equivalent electron distribution. This is due to the symmetry in the reciprocal lattice space. Moreover, the LCAO coefficients of carbon B in eq. (2) change by the band (conduction or valence) and 2D wavevector. That is the reason why the spiral pattern appears at the band edge and the running direction change by the sign of bias voltage.
The interference at the band edge occurs for a single condition of the wave vector, which is the reflection from bottom k to $-k$ [Fig. 9(b)]. The images at the conduction band edge are given in Fig. 9(e) and 9(f), which are obtained with $\eta = 0$ and π, respectively. Similar to the case of the metallic CNT, the real and imaginary parts of the wavefunction appear in these interference images according to the phase shift of the reflection. However, these images show similar distributions and seem to be the mixing of Fig. 8(b)-(e). The reason why the clear pattern is not observed is that the band edge energy is well separated from Fermi level. When the electron energy is close to Fermi level, the wavelength is ~3a (Fermi wavelength). On the other hand, the wavelength at conduction band bottom is shorter than 3a. Therefore, the periodicity of LCAO coefficient $\exp(i\boldsymbol{k}\cdot\boldsymbol{R})$ does not agree with that of the unit cell of the graphene sheet. Hence, the interference image shows a modulation with a long periodicity.

3.3 Comparison of simulated results and STM images

We now compare the observed STM images near the end-cap of a CNT and the simulated images. We concentrate on the images of a conduction band ($V_{sample}>0$ in STM observation). We consider a standard Bloch state based on the graphene sheet using the eq. (2) shown above and the parameter of $\boldsymbol{k}_{min}$.
The bonding and antibonding band corresponds to + and –, respectively. If we consider the antibonding band at the Γ point, the carbon atoms have an alternative phase that gives – in eq. (2).

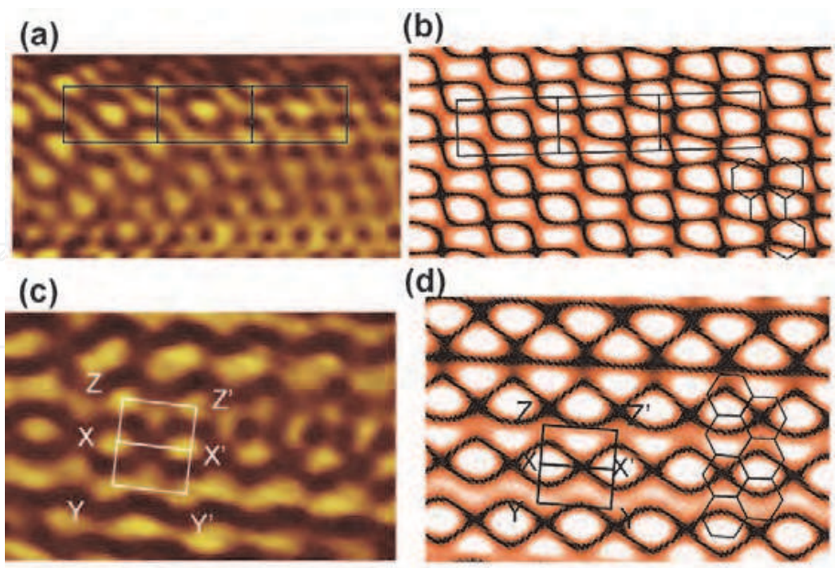

Fig. 10. Comparison of STM image and simulation (a)(b) Comparison of an STM image (same as Fig. 4(a)) and a simulation result for a CNT of (28, -13). Superimposed rectangles are included as a guide to the eye of the equivalent site. (c)(d) Comparison for (15,-1). XX′, YY′ and ZZ′ indicate the comparison.

The interference of the wavefunctions is estimated by using eq. (9) We fixed η at π for the entire simulation, which is based on the result of a theoretical calculation of an electronic state at end-cap (Yaguchi et al., 2001). However, the calculated interference pattern is not sensitive to the changes of η. The Bloch states of $\boldsymbol{k}_1$ and $\boldsymbol{k}_2$ should have the same energy for elastic scattering. This condition limits the allowed wavevectors, and the combination of $\boldsymbol{k}_{min}$ and $-\boldsymbol{k}_{min}$ satisfies this condition. Though $\boldsymbol{k}_{min}$ is close to **K**, they do not coincide. A complex interference pattern is produced depending on the relative position of $\boldsymbol{k}_{min}$ around K. The calculated ρ is expressed by mapping the amplitude two dimensionally.

We first compare an STM image and a simulation result for a CNT whose chirality is close to an armchair. The experimental and simulation results are shown in Fig. 10(a) and 10(b), respectively; the former is a part of Fig. 4(a). The scale and alignment of the tube axis are common in two panels. To clarify the similarity between Fig. 10(a) and 10(b), three rectangles ($3\boldsymbol{a}\times\sqrt{3}\boldsymbol{a}$) are superimposed. Bright spots at the four corners and the center of the rectangle are visible both in the image and simulation. In addition, wavy lines are reproduced well.

$\boldsymbol{k}_{min}$ is slightly off **K**, which forms a modulation with a longer periodicity. In the simulation, this can be seen as a gradual change from a wavy line to a dot-like feature in the right-hand side of the panel. This is also seen in the STM image in Fig. 4(a); the wavy lines become dot-like near the end-cap.

The results for a zigzag-type CNT are shown in Figs. 10(c) and 10(d). $\boldsymbol{k}_{min}$ is rotated ~30° from the tube-axis direction. Characteristic wavy lines along the tube-axis direction and aligned bright spots perpendicular to the tube-axis are well reproduced. XX′, YY′ and ZZ′ are shown in both panels as an eye-guide, with a length of $\sqrt{3}\boldsymbol{a}$ and a separation of $\boldsymbol{a}$. Good agreement between the STM image and the simulation results are seen at each point. Since there expected a long-range modulation in the image along YXZ direction, the features along YY′ and those along ZZ′ in the STM images are not identical.

4. Future perspective of interference imaging of CNT

Here we try to observe variations in the interference pattern in a systematic manner; in other words, we attempt to obtain the relationship between $\boldsymbol{k}_{min}$ and the interference pattern. (Furuhashi et al., 2008) $\boldsymbol{k}_{min}$ can be expressed as a relative position from $\boldsymbol{K}$, *i.e.*, $\Delta\boldsymbol{k}=(\boldsymbol{k}_{min}-\boldsymbol{K})$ which can be specified by the length $|\Delta\boldsymbol{k}|$ and an angle from a symmetric line (ϕ). In Fig. 11(a), solid circles show five $\boldsymbol{k}_{min}$ points with the same $|\Delta\boldsymbol{k}|$ and different ϕ from the direction of $\boldsymbol{\Gamma K}$. For these $\boldsymbol{k}_{min}$ points, we calculated the interference pattern by using eq. (3). The results for an unoccupied state are shown in Fig. 11(b).

For $\phi=0°$, $\boldsymbol{k}_{min}$ is located on the $\boldsymbol{MK}$ line. The Bloch states in the unoccupied state have a *positive* combination in eq (3). This is because they are on the line from $\boldsymbol{\Gamma}$ to $\boldsymbol{K}$, and $\boldsymbol{k}_{min}$ is beyond $\boldsymbol{K}$. Thus, the unoccupied wave function is positioned on the band that has a bonding character at $\boldsymbol{\Gamma}$. The sign of eq. (3) is positive, and consequently, wavy lines are clearly observed. The periodicity along arrow A in Fig. 11(b) ($\boldsymbol{\Gamma K}$ direction) is deviated from $3\boldsymbol{a}$, but the periodicity along arrow B ($\boldsymbol{\Gamma M}$ direction) is fixed at $\sqrt{3}\,\boldsymbol{a}$.

For $\phi=60°$, $\boldsymbol{k}_{min}$ is on the symmetry line of $\boldsymbol{\Gamma K}$; this is similar to the $\phi=0°$ case but $\boldsymbol{k}_{min}$ does not reach $\boldsymbol{K}$. As the reverse case of $\phi=0°$, the Bloch state corresponds to a negative combination in eq. (3). With this configuration, the wavy patterns disappear and the periodic lattice is visible. The periodicity in the $\boldsymbol{\Gamma K}$ direction is shifted from $3\boldsymbol{a}$, however, modulation with a long periodicity is not visible.

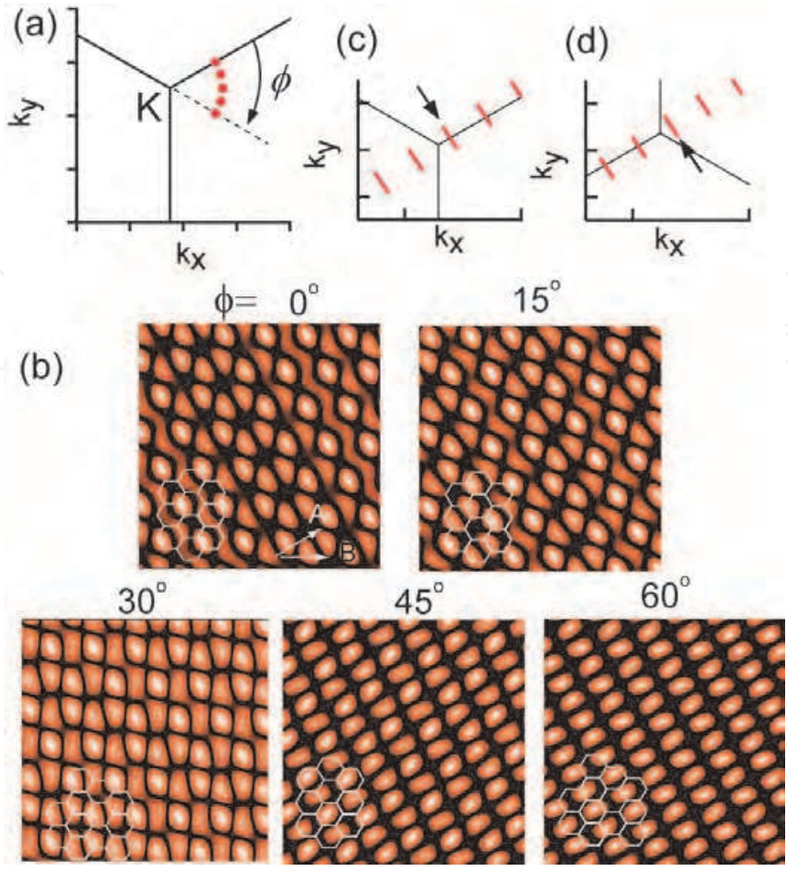

Fig. 11. Interference catalogue with chiral vector (a) Assumed $\boldsymbol{k}_{min}$ positions for a simulation of the interference pattern, specified by the angle from the ΓK direction, ϕ=0°, 15°, 30°, 45°, and 60° and distance from K. (b) Simulated images for each ϕ. The $\boldsymbol{k}_{min}$ used for the simulation is set close to the direction shown by the arrow. Though there are six equivalent k points in a Brillouin zone with a same energy, the interference pattern is also aligned in this direction. (c), (d) Brillouin zones and the short lines of allowed $\boldsymbol{k}$ of the CNT of (c) (15, -1) and (d) (16, -1). The points closest to K and K' are depicted by arrows.

The pattern of ϕ=30° is a mixture of the former two cases. Wavy lines are clearly observed in some parts, but are not symmetric and show long-range modulation. This corresponds to the modulation observed in Fig. 4(a).

If the chirality is close to the armchair, $\boldsymbol{k}_{min}$ expectedly appears at ϕ~30°. This can be understood by using the Brillouin zone in Fig. 5(b). For armchair CNTs, the translational vector is close to the vertical direction in Fig. 11(a). Since $\boldsymbol{k}_{min}$ is specified by the cross point of the translational vector and its perpendicular line through K, it is located in the horizontal direction from $\boldsymbol{K}$ and corresponds to ϕ~30°. With similar consideration, $\boldsymbol{k}_{min}$ can be found at ϕ~0° or 60° for a zigzag CNT.

It is intriguing to see that a large change in the interference pattern is caused by a small change in the chiral vector. A clear example of this can be seen for the zigzag CNT, and we show a comparison for cases of (15, -1) and (16, -1). In Fig. 11(c) and (d), we show the allowed $\boldsymbol{k}$ as short bars for (15, -1) and (16, -1), respectively. The positions of $\boldsymbol{k}_{min}$ for both cases are indicated by arrows, which are on the reverse sides of $\boldsymbol{K}$. In the Brillouin zone, the

former and latter are located close to the line of $\phi=0^o$ and $\phi=60^o$, respectively. The expected difference in the interference patterns for $\phi=0^o$ and $\phi=60^o$ is clearly seen in Fig. 11(b); wavy lines are visible in the former case but disappear in the latter case. In chiral vector determination, the observation of interference patterns can play a complementary role to direct observations of the hexagonal network, as electron and photon diffraction techniques have contributed to structure determination of the materials.

We have focused our discussion on semiconducting CNTs. Similar discussions can be applied for metallic CNTs. However, as were pointed out by Kane and Mele (Kane et al., 1999), two branches of E(k) curves exist in the band structure near E_f, which makes the interference patterns more complicated than those of semiconducting CNTs.

5. Conclusion

We have discussed the internal structure of the CNT by experimental scanning tunneling microscopy observation and theoretical simulations, focusing on the interference pattern observed near the end-cap of the CNT. We analyzed the complex shape of the pattern for the understanding of the underlying physics, which is an appearance of the wavefunctions. It is also intended for the application of the interference observation to the determination of the chirality, which is one of the most important parameters for the CNT, utilizing the sensitivity of the reflection patterns. Simulations were executed both by molecular orbital calculation and the Bloch theorem. In the latter, a two-dimensional interference of the wavefunctions was calculated assuming the superposition of the forward and backward waves that has equivalent electron energy.

The observed STM images showed a complex pattern at the end-cap of the CNT, which was typically observed for the area of ~6 nm from the end. For the armchair CNT, cranked wavy lines and oval shaped spots with the periodicity of $\sqrt{3}\,a$ were commonly observed along the armchair direction (a is the unit vector length of the graphene sheet; a=0.25 nm). The oval spots were also observed in the CNT with the chirality between the armchair and zigzag, whose periodicity was ~$3a$ in the zigzag direction.

These structures were well reproduced both by the molecular orbital and the Bloch theorem calculations. The simulation clearly demonstrated the expected patterns both for metallic and semiconductive CNTs revealing the wavefunctions that constructed the interface patters. In addition, the interference patterns were successfully catalogued as a function of the chirality. An intriguing finding was that a minute change in the chirality modified the interference pattern considerably. The sensitivity of the interference pattern with the chirality differences demonstrated the possibility of the use of this technique for the precise determination of the chirality of the CNTs.

6. Acknowledgment

TK acknowledge support from KAKENHI (22241026), and “R&D promotion scheme funding international joint research” promoted by NICT (National Institute of Information and Communication Technology), Japan..

7. References

Joachim, C. (2000). Electronics using hybrid-molecular and mono-molecular devices. *Nature*, 408, 541-548

Tans, S. J. (1997). Individual single-wall carbon nanotubes as quantum wires. *Nature*, 386, 474-477

Saito, R. Physical Properties of Carbon Nanotubes (Imperial College Press, London, 1998).

Javey, A. (2003). Ballistic carbon nanotube field-effect transistors. *Nature*, 424, 654-657

Lemay, S. G. (2001). Two-dimensional imaging of electronic wavefunctions in carbon nanotubes. *Nature*, 412, 617-620

Venema, L. C. (1999). Imaging electron wave functions of quantized energy levels in carbon nanotubes. *Science*, 283, 52-55

Ouyang, M. (2002). One-dimensional energy dispersion of single-walled carbon nanotubes by resonant electron scattering. *Phys. Rev. Lett.*, 88, 66804

Lee, J. (2004). Real Space Imaging of One-Dimensional Standing Waves: Direct Evidence for a Luttinger Liquid. *Phys. Rev. Lett.*, 93, 166403-166404

Furuhashi, M. (2007). Direct Observation of Molecular Orbital at Carbon Nanotube End *Japanese Journal of Applied Physics*, 46, L161-164

Furuhashi, M. (2008). Chiral Vector Determination of Carbon Nanotubes by Observation of Interference Patterns Near the End Cap. *Phys. Rev. Lett.*, 101, 185503

Nikolaev, P. (1999). *Chem. Phys. Lett.* , 313, 91

Batra, I. P. (1987). A study of graphite surface with stm and electronic structure calculations. *Surf. Sci.*, 181, 126-138

Venema, L. C. (2000). Spatially resolved scanning tunneling spectroscopy on single-walled carbon nanotubes. *Phys. Rev. B*, 62, 5238-5244

Meunier, V. (1998). Tight-binding computation of the STM image of carbon nanotubes. *Phys. Rev. Lett.*, 81, 5588-5591

Xhie, J. (1991). Superstructures on graphite near platinum particles. *J. Vac. Sci. Technol. B*, 9, 833-836

Kobayashi, Y. (2005). Observation of zigzag and armchair edges of graphite using scanning tunneling microscopy and spectroscopy. *Phys. Rev. B*, 71, 193406

Kim, H. (2005). Local electronic density of states of a semiconducting carbon nanotube interface. *Phys. Rev. B*, 71, 235402

Rubio, A. (1999). *Phys. Rev. Lett.*, 82., 3520

White, C. T. (1998). Density of states reflects diameter in nanotubes. *Nature*, 394, 29-30

Kane, C. L. (1999). Broken symmetries in scanning tunneling images of carbon nanotubes. *Phys. Rev. B*, 59, R12759

Stewart, J. J. P. (1989). Optimization of Parameters for Semiempirical Methods .1. Method. *J. Comput. Chem.*, 10, 209-220

Stewart, J. J. P. (1989). Optimization of Parameters for Semiempirical Methods .2. Applications. *J. Comput. Chem.*, 10, 221-264

Stewart, J. J. P. (1991). Optimization of Parameters for Semiempirical Methods .3. Extension of Pm3 to Be, Mg, Zn, Ga, Ge, as, Se, Cd, in, Sn, Sb, Te, Hg, Tl, Pb, and Bi. *J. Comput. Chem.*, 12, 320-341

Stewart, J. J. P. (1990). Special Issue - Mopac - a Semiempirical Molecular-Orbital Program. *Journal of Computer-Aided Molecular Design*, 4, 1-45

Meunier, V. (2004). Scanning tunnelling microscopy of carbon nanotubes. *Philosophical Transactions of the Royal Society of London. Series A: Mathematical, Physical and Engineering Sciences*, 362, 2187-2203

Clauss, W. (1999). Electron backscattering on single-wall carbon nanotubes observed by scanning tunneling microscopy. *EPL (Europhysics Letters)*, 47, 601

Yaguchi, T. (2001). Electronic states in capped carbon nanotubes. *J. Phys. Soc. Jpn.*, 70, 1327-1341

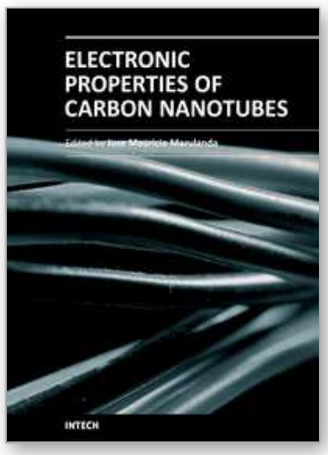

Electronic Properties of Carbon Nanotubes

Edited by Prof. Jose Mauricio Marulanda

ISBN 978-953-307-499-3
Hard cover, 680 pages
Publisher InTech
Published online 27, July, 2011
Published in print edition July, 2011

Carbon nanotubes (CNTs), discovered in 1991, have been a subject of intensive research for a wide range of applications. These one-dimensional (1D) graphene sheets rolled into a tubular form have been the target of many researchers around the world. This book concentrates on the semiconductor physics of carbon nanotubes, it brings unique insight into the phenomena encountered in the electronic structure when operating with carbon nanotubes. This book also presents to reader useful information on the fabrication and applications of these outstanding materials. The main objective of this book is to give in-depth understanding of the physics and electronic structure of carbon nanotubes. Readers of this book should have a strong background on physical electronics and semiconductor device physics. This book first discusses fabrication techniques followed by an analysis on the physical properties of carbon nanotubes, including density of states and electronic structures. Ultimately, the book pursues a significant amount of work in the industry applications of carbon nanotubes.

InTech Europe
University Campus STeP Ri
Slavka Krautzeka 83/A
51000 Rijeka, Croatia
Phone: +385 (51) 770 447
Fax: +385 (51) 686 166
www.intechopen.com

InTech China
Unit 405, Office Block, Hotel Equatorial Shanghai
No.65, Yan An Road (West), Shanghai, 200040, China
中国上海市延安西路65号上海国际贵都大饭店办公楼405单元
Phone: +86-21-62489820
Fax: +86-21-62489821

IntechOpen